Experimental Analysis of Reinforced Concrete Deep Beams with Circular Openings Strengthened by GFRP and Steel Bars

M. Mirzaie Aliabadi[1] · P. Homami[1] · A. Massumi[1]

Abstract

This study investigated the behavior of deep beams with openings that have been reinforced with GFRP and steel bars. A total of 14 reinforced concrete deep beams having a rectangular cross-section of 150×500 mm and a total length of 1600 mm were constructed with or without openings and tested up to failure under a four-point bending test. The parameters studied were the opening diameter (140 and 240 mm), number and location of the openings and the shear span-to-depth ratio (a/d). These beams were divided into Group I ($a/d = 0.9$) and Group II ($a/d = 0.5$). In each group, one beam had no opening to serve as the control beam. Two beams had one opening in the shear area, two had one at the mid-span of the beam and two had two openings, one on each side of the beam. Finite element modeling with strong correlation with the laboratory results was performed. The results showed that an increase in a/d caused a decrease in the final strength of the beam. The number of openings and their locations on the load transfer path were factors that significantly reduced the ultimate load borne by the beam. Comparison of the test results with the relations provided in design regulations indicated that the ultimate strengths of the beams were higher than the values obtained from the regulations. On average, the values calculated based on ACI 318–19 and Canadian S806-2012 were 86.95 and 55.55% lower than the test results, respectively.

Keywords Reinforced concrete · Deep beam · GFRP · Failure mode · Crack propagation

1 Introduction

A beam with a clear span that is less than four times the overall depth of the section is classified as a deep beam [1, 2]. reinforced concrete (RC) Deep beams are commonly used in high-rise structures, bridges, dams, reservoirs, shear walls, floor diaphragms, slabs and transmission girders in marine structures [3, 4]. The behavior of these types of beam indicates that the Euler–Bernoulli theory [5] does not apply to them; their design differs from ordinary beams [6].

The substantial height of deep beams require them to have an opening for the passage of facilities; however, the creation of an opening in the beam will reduce its bearing capacity. The factors affecting the behavior of RC deep beams with openings include the shape and dimensions of the beam section (rectangular, T-shaped), concrete strength, arrangement and number of longitudinal and transverse reinforcements, ratio of the shear depth to the effective height of the beam [7], type and location of load application as well as the dimensions, location and geometric shape of the opening [8].

Research on beams with openings date back to 1967. Initially, researchers focused on RC beams with rectangular openings [9]. The results indicated that creation of an opening in the shear areas of the beams significantly decreased their load-bearing capacity [10–13]. Past research has focused on the use of composite materials to improve the behavior of deep beams with openings [14–16]. Because of the tensile characteristics of GFRP rebars, it is possible to use them instead of steel rebars [17, 18], but this possibility generally has not been considered for deep beams with openings.

Mohammad et al. have studied the behavior of deep beams with openings in the critical shear zone in the range of strut lines. The variables included in this research consist of the shape and location of the opening. After modeling the beams using finite element software and comparing with the laboratory results, it was determined the presence of the two openings in the same span caused 38% reduction in failure

✉ P. Homami
homami@khu.ac.ir

1 Department of Civil Engineering, Faculty of Engineering, Kharazmi University, Tehran, Iran

Springer

load irrespective of the shape of opening. For the second opening layout having one opening in each span, the reduction was slightly higher but almost the same for the two shapes of openings (41% for circular and 45% for rectangular opening) [19].

Ahmad et al. investigated eight continuous deep beams with and without openings. The variables were the ratio of transverse reinforcement and the position, height, and width of the opening. After modeling the samples and comparing with the test results, it was determined that the failure mode of two-span continuous deep beams depends mainly on the position and size of the opening in the shear span and the failure occurs in the diagonal strut between the support and the applied force through the opening edges [20].

Manasa et al. evaluated 12 deep reinforced concrete beams (conventional concrete and fiber concrete) with and without openings under bending experimentally and numerically. Numerical analysis was done using Ansys software and the results were in good agreement with the laboratory results. From the experimental test results, it was observed that the addition of fibre leads to significant increase in failure load. It is also noticed that the opening disrupts the crack pattern by deviating the natural load path of the crack [21].

Jacob et al. [22] investigated the behavior of seven deep concrete beams reinforced with GFRP and steel rebars with and without openings. They evaluated the crack patterns, failure modes and the effects of openings on beam resistance. They showed that the strength of deep concrete beams without an opening were similar when reinforced with GFRP or steel rebars. For beams with openings, those reinforced with GFRP showed less resistance than those with openings reinforced with steel rebars.

Arabasi and Al-Madawi [23] evaluated 12 RC deep beams with openings that had been reinforced with GFRP rebars. One beam did not have an opening. The other beams each had an opening in the shear zone. The opening height, concrete strength and rebar arrangement in the discontinuity area of the beam were the variables evaluated. The results showed that an increase in the height of the opening caused a decrease in the strength of the beam. A diagonal arrangement of rebars had a positive effect on increasing the capacity of the beam. These values also were calculated using relations from American and Canadian regulations and were compared with the laboratory results. They indicated that the results from the relations in the regulations were conservative.

Margin and Prasanna [24] investigated the laboratory behavior of six deep RC beams with openings. Four beams were reinforced with GFRP rebars and two beams were reinforced with steel rebars. The ultimate capacity of the beams and the number of cracks and method of their formation and expansion were evaluated. The laboratory results were compared with those of the models developed in FE software. They showed that the ultimate capacity of the samples reinforced with GFRP rebars was lower than for the beams reinforced with steel rebars.

The shear behavior of RC members is complex because it relates to different factors [25–27]. The level of complexity doubles for deep beams because of the manner of load transfer and the non-linear strain distribution in the beam section [28, 29]. With the formation of cracks, the beam has been shown to act as a tied arch [30], known as a strut-and-tie model (STM). International codes such as ACI 318–19 [31], AASHTO LRFD [32], Eurocode 2 [33] and FIB MC2010 [34] allow the design of deep beams using the STM method.

Due to the significant increase in the power of finite element software as well as the exorbitant cost of building and testing samples in real dimensions, many researchers [35, 36] have turned to conducting their research based on modeling. However, the completion of the library of software specifications and how cracks are formed in the elements and the type of rupture need to be matched with the laboratory data. Therefore, conducting laboratory tests and modeling at the same time seems necessary [37, 38]

The current study provides information about the structural performance of RC deep beams with and without openings and the strength of the GFRP and steel rebars to better understand the failure mechanism of such elements. A review of previous research and design regulations of concrete structures has found that there is little information on the behavior of deep beams with openings that have been reinforced with composite bars. The results of the current research can offer new information for future research about the behavior of deep beams with openings that have been strengthened with GFRP rebars and the relationships related to them. This research contributes to a laboratory study on the behavior and shear capacity of 14 deep beams with openings that had been reinforced with longitudinal GFRP rebars and transverse steel rebars. The variables considered were the ratio of the shear depth to the effective height of the beam, as well as the dimensions, number and location of the openings were considered. The laboratory results then were compared with the regulatory formulas. Finite element modeling was performed to confirm the numerical accuracy of the samples, and a strong correlation was found between the numerical and laboratory results.

2 Experimental Program

2.1 Test Specimens and Materials

Fourteen RC deep beams with and without openings were tested up to failure. All beams were 150 mm in width, 500 mm in depth and 1600 mm in length. The variables considered were the ratio of the shear depth to effective height of the

Table 1 Designations of tested deep beams

Group	Sample number (Ni)	Number of openings	Opening position	Opening diameter (cm)
I	i = 1, 3, 5, 7, 9, 11, 13	H0	–	–
		H1	C, L	D24, D14
II	i = 2, 4, 6, 8, 10, 12, 14	H2	L&R	

beam and the dimensions, number and location of the openings. The beams were divided into two groups. In Group I, the shear depth to effective height ratio of the beam was 0.9 ($a/d = 0.9$). In Group II, this ratio was $a/d = 0.5$. In each group, one beam without an opening was used as the control beam and the remaining six beams had one or two openings. Table 1 lists the designations of the beams according to the diameter of the openings (140 mm (D14) or 240 mm (D24)), their location (mid-span of beam (C) or shear span (L, L&R)) and their number (0 (H0), 1 (H1) or 2 (H2)). The samples with odd numbers belong to Group I and the samples with even numbers belong to Group II.

All deep beams were designed with two GFRP rebars of 10 mm in diameter for the tension zone. The GFRP bars were positioned in the compression zone of the beam but, because of the characteristics of composite bars, they did not serve a structural function in that area. They were only used for confinement of the transverse rebars. The behavior of the GFRP rebars was elastic, their tensile strength was 950 MPa and their modulus of elasticity was 53 GPa.

In all samples, steel rebars of 8 mm in diameter were used for shear reinforcement. In the design of all beams, transverse bars were placed 50 mm apart and up to 150 mm from the opening and supports, the yield stress of the steel rebars was 275 MPa and the modulus of elasticity was 200 GPa. To improve bonding the GFRP rebars [39, 40] in all samples, the restraint length from the sides of the support was set at 300 mm. This part of the beam played no load bearing role. Figure 1 shows the reinforcement details for a typical test beam.

Depending on the dimensions of the cross-section of the beam and to facilitate its implementation and vibration, fine-grained concrete was used. To ensure control over the concrete specifications and minimize uncertainty, all samples were concreted in a single operation (Fig. 2a). The web openings in the beams were created using polyester cylinders with diameters of 140 or 240 mm with a height of 150 mm (Fig. 2b).

Table 2 shows the location of the opening and the number and arrangement of longitudinal and transverse rebars. The compressive strength of the concrete was determined on 15 cm^3 samples (Fig. 2d) over lifespans of 3, 7 and 28 days. To expedite the increase in concrete strength, steam pressure was applied to all beams for 8 h (Fig. 2e). The beams then were carefully maintained for 28 days. The cubic samples were also steamed for one day next to the beams and then were submerged in a pool of water (Fig. 2c). Normal-weight concrete with an average cylindrical compressive strength (f_c') of 29 MPa at 28 days was used to cast the beams.

2.2 Test Setup and Instrumentation

The four-point bending test was used on all specimens under simply supported conditions. All samples were tested individually up to failure. The setup of a typical deep beam is shown in Fig. 3. The supports were located 500 mm from the sides relative to the mid-span of the beam. The distance between the application of the load and mid-span of the beam according to a/d for Group I was 95 mm and for Group II was 275 mm.

In each experiment, five LVDTs were used to measure changes in length and one strain gauge was used to investigate the behavior of the GFRP rebars located in the tensile zone of the beam (Fig. 3a). LVDT1 and LVDT5 were installed obliquely in line with the location of load application to the support to allow measurement of changes in this area during loading. LVDT3 was installed at the bottom at the mid-span of the beam to record displacement of that part of the beam. To control the behavior of the beam, LVDT2 and LVDT4 were installed at the lower part of the beam parallel to the point of loading.

A hydraulic jack with a capacity of 150 tons was used for testing. The loading speed was 1 mm/min. All information was recorded on a data logger. Cracks formed on the beam up to the moment of failure. The beams were photographed at each stage. All the experiments were done in the laboratory of the Tarbiat Modares University (Fig. 3b). Steel plates of $150 \times 150 \times 20$ mm were placed under the applied load as well as at the supports to prevent local stress concentration.

3 Results

3.1 Initial Crack and Ultimate Load Capacity

The cracks in the samples were examined by visual inspection during the test. The testing was stopped several times to record changes in the cracks and so that videos could be
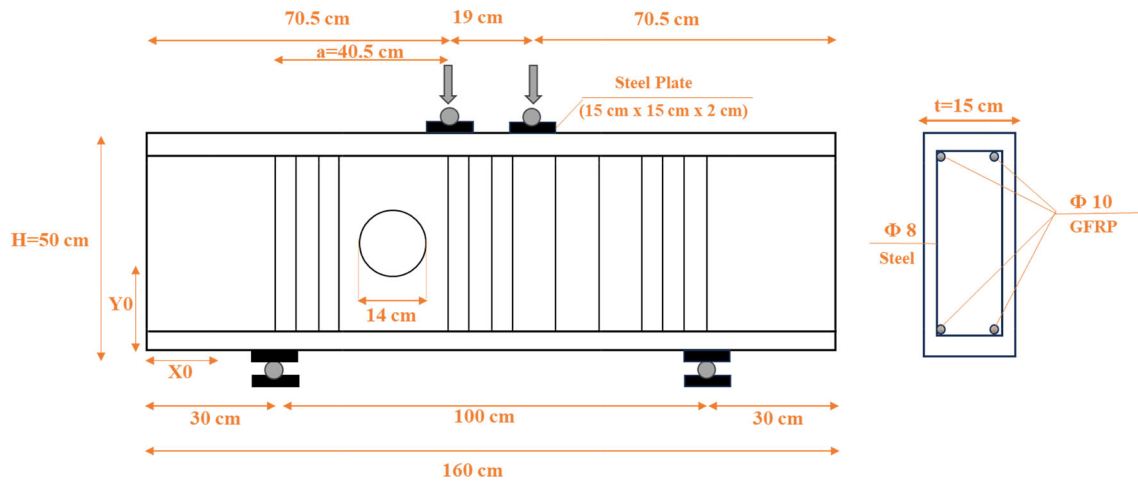
Fig. 1 Reinforcement features for a typical test beam (N3H1LD14)

Fig. 2 Construction of specimens: **a** concrete casting; **b** polystyrene cylinders; **c** curing tank with cubic concrete samples; **d** cubic concrete samples; **e** curing beams under steam
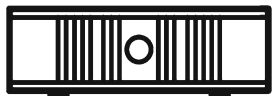
taken. These were reviewed and the manner of spreading of the cracks was identified.

It is known that the behavior of concrete in tension is not suitable. With the formation of the initial main crack in the tension zone of the beam, the tensile load was carried by the longitudinal bars. A strain gauge was installed on the GFRP rebars to increase the accuracy of determination of the amount of loading relative to the formation of the initial crack in the tensile zone of the beam. Table 3 summarizes the initial crack information and ultimate loads for each beam.

Table 3 reveals that the percentage of initial-crack load to ultimate load was 7.6 to 49.6% for Group I and 14.7 to 35.1% for Group II. At the specified intervals, it can be seen that the shear length to beam depth ratio had a greater effect than the dimensions of the opening on the ultimate strength of the beam.

Table 2 Number and arrangement of bars and locations of openings

Sample name	Specimen	Opening coordinates (mm)		Transverse rebars (steel)	Longitudinal rebars (GFRP)
		Y_0	X_0	Number and diameter	Number and diameter
N1H0 N2H0		–	–	$14\phi8$	$2\phi10$
N3H1LD14 N4H1LD14		250	570	$14\phi8$	$2\phi10$
N5H1CD14 N6H1CD14		250	800	$16\phi8$	$2\phi10$
N7H2L&RD14 N8H2L&RD14		250	570,1030	$13\phi8$	$2\phi10$
N9H1LD24 N10H1LD24		250	620	$13\phi8$	$2\phi10$
N11H1CD24 N12H1CD24		250	620	$16\phi8$	$2\phi10$
N13H2L&RD24 N14H2L&RD24		250	620,980	$10\phi8$	$2\phi10$

3.2 Crack Patterns and Failure Modes

In the Group I test results, the initial crack in N1H0 formed vertically at the mid-span of the beam and then spread and extended to half the depth of the beam. Shear cracks then started to form and the initial bending crack increased in size. The shear cracks spread to the top of the beam to the loading point. Gradually, the cracks spread towards the support areas and diagonal cracks formed at the loading points on the right and left sides of the beam, respectively. Before failure of the beam, some of the surface layers of concrete spalled on the right support where the load had been applied (Fig. 4a).

The initial crack in N3H1LD14 formed in shear at the bottom of the opening and then spread into the opening. Next, a crack formed in line with the initial crack at the top of the opening toward the loading point and the diameter of the opening increased. Vertical cracks then formed in the lower area of the beam. As the force increased, diagonal cracks were observed on the right side of the beam, which finally failed with the collapse of the opening (Fig. 4b).

The initial crack in N5H1CD14 formed vertically at the mid-span of the beam below the opening. Shear cracks then were observed around the opening and a crack formed at the top of the opening. The shear cracks propagated towards the opening. As the load increased, diagonal cracks formed from the loading point to the supports on the right and left sides of the beam. The beam finally failed on the right side of the beam because of the widening depth of the shear cracks (Fig. 4c).

The location of the opening in the area of shear played a major in the load transfer. The initial cracks formed on the sides of the N7H2L&RD14 and propagated towards the opening. Gradually, cracks developed above the opening and along the initial cracks. As the load increased, flexural cracks formed in the tensile region of the beam. Finally, the beam failed with the collapse of the opening on the left side of the beam (Fig. 4d).

The initial crack in N9H1LD24 was a shear crack that formed at the bottom of the opening. Next, a crack formed at the top of the opening in line with the initial crack. As
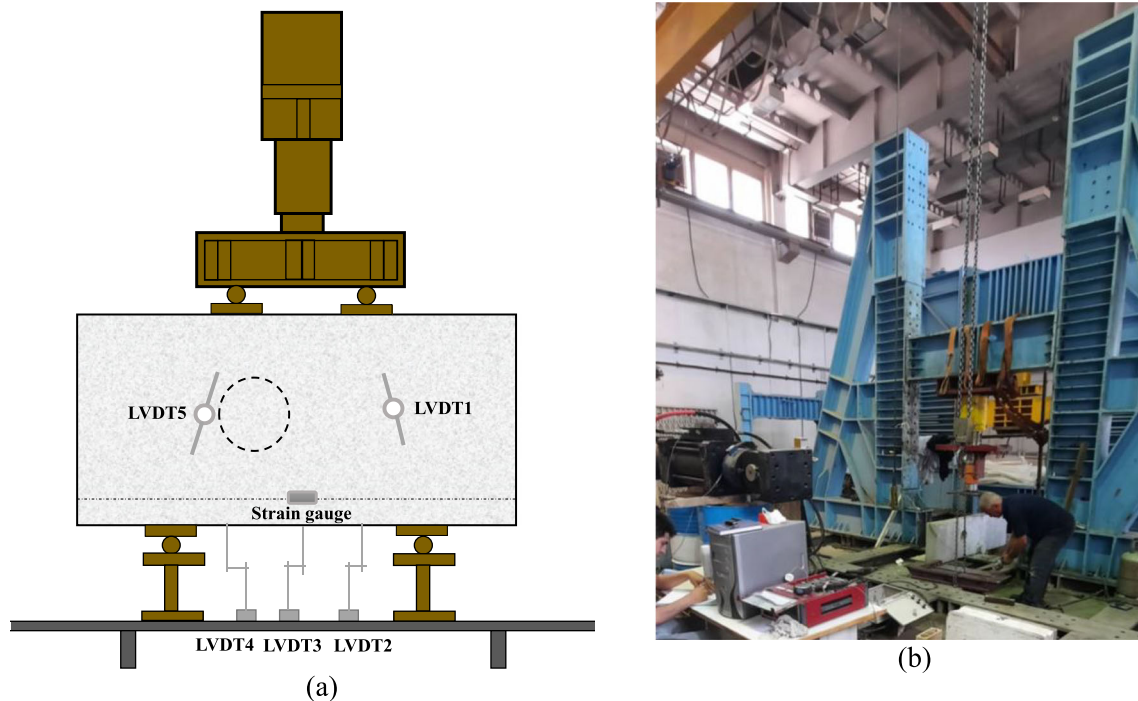
Fig. 3 Setup of typical test beams: **a** location of LVDTs and strain gauge; **b** structural laboratory at Tarbiat Modares University

Table 3 Test results for initial cracking and ultimate loads

| Group	Specimen	Load at initial crack (P_{cr}) kN	Location of initial crack	Type of crack	Ultimate load (P_U) kN	$\frac{P_{cr}}{P_{U}v}$ %
Group I	N1H0	42	Mid-span of beam	Flexural	549	7.6
	N3H1LD14	60	Below and toward opening	Shear	173	34.6
	N5H1CD14	56	Mid-span of beam toward opening	Flexural	605	9.2
	N7H2L&RD14	80	Below and toward opening	Flexural-Shear	161	49.6
	N9H1LD24	24	Below and toward opening	Shear	135	17.7
	N11H1CD24	75	Mid-span of beam toward opening	Flexural	575.5	13
	N13H2L&RD24	45.5	Mid-span of beam toward left	Flexural	132	34.4
Group II	N2H0	100	Mid-span of beam	Flexural	680	14.7
	N4H1LD14	207	Below and toward opening	Shear	590	35.1
	N6H1CD14	173	Below and toward opening	Flexural-Shear	680	25.4
	N8H2L&RD14	88.5	Mid-span of beam	Flexural	560	6.3
	N10H1LD24	120	Mid-span of beam	Flexural	540	22.2
	N12H1CD24	174	Mid-span of beam toward opening	Flexural	608	28.6
	N14H2L&RD24	89	Mid-span of beam toward right	Flexural	500	17.6
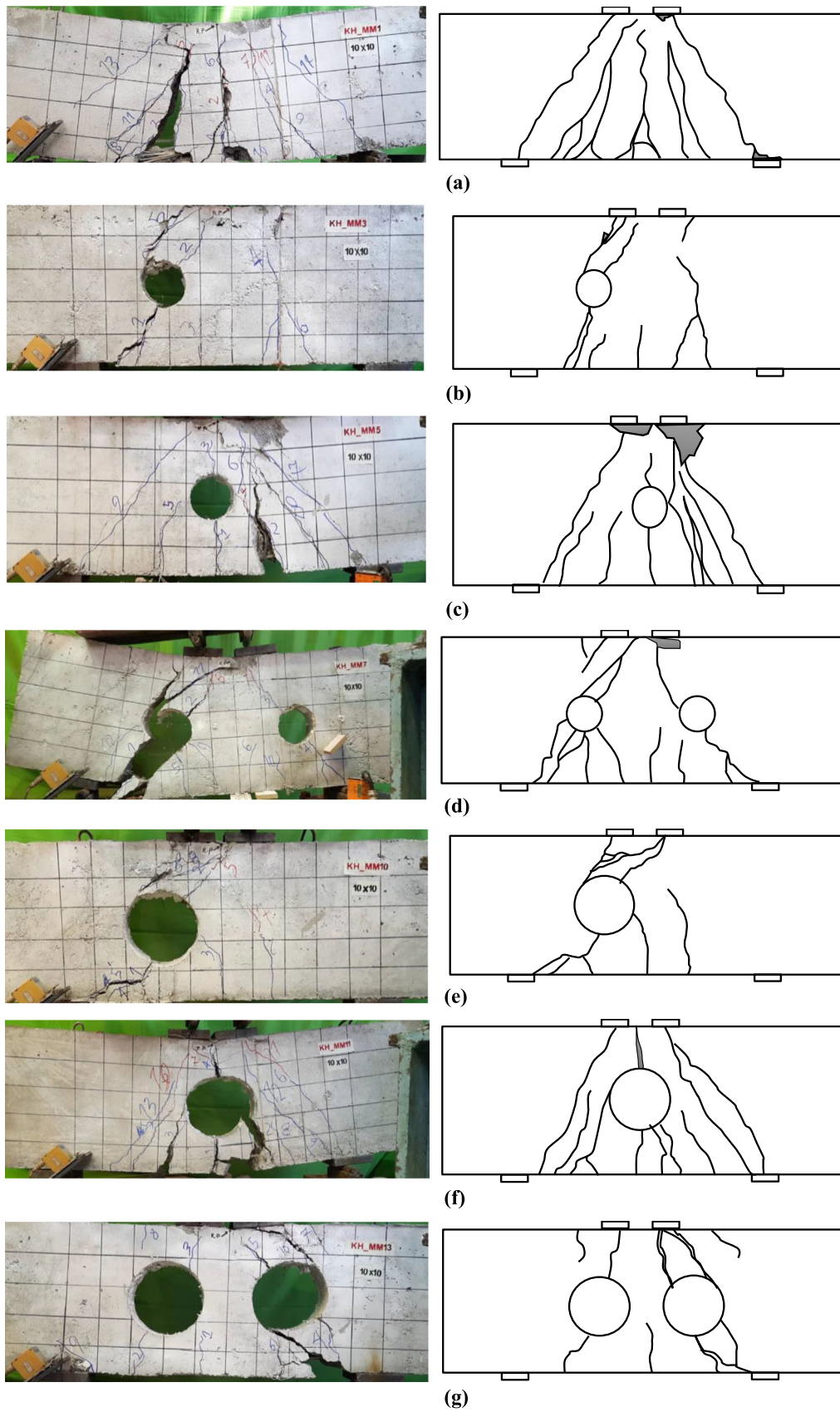
Fig. 4 Crack patterns and failure modes of Group I: **a** N1H0; **b** N3H1LD14; **c** N5H1CD14; **d** N7H2L&RD14; **e** N9H1LD24; **f** N11H1CD24; **g** N13H2L&RD24

Fig. 5 Crack patterns and failure modes in Group II: **a** N2H0; **b** N4H1LD14; **c** N6H1CD14; **d** N8H2L&RD14; **e** N10H1LD24; **f** N12H1CD24; **g** N14H2L&RD24
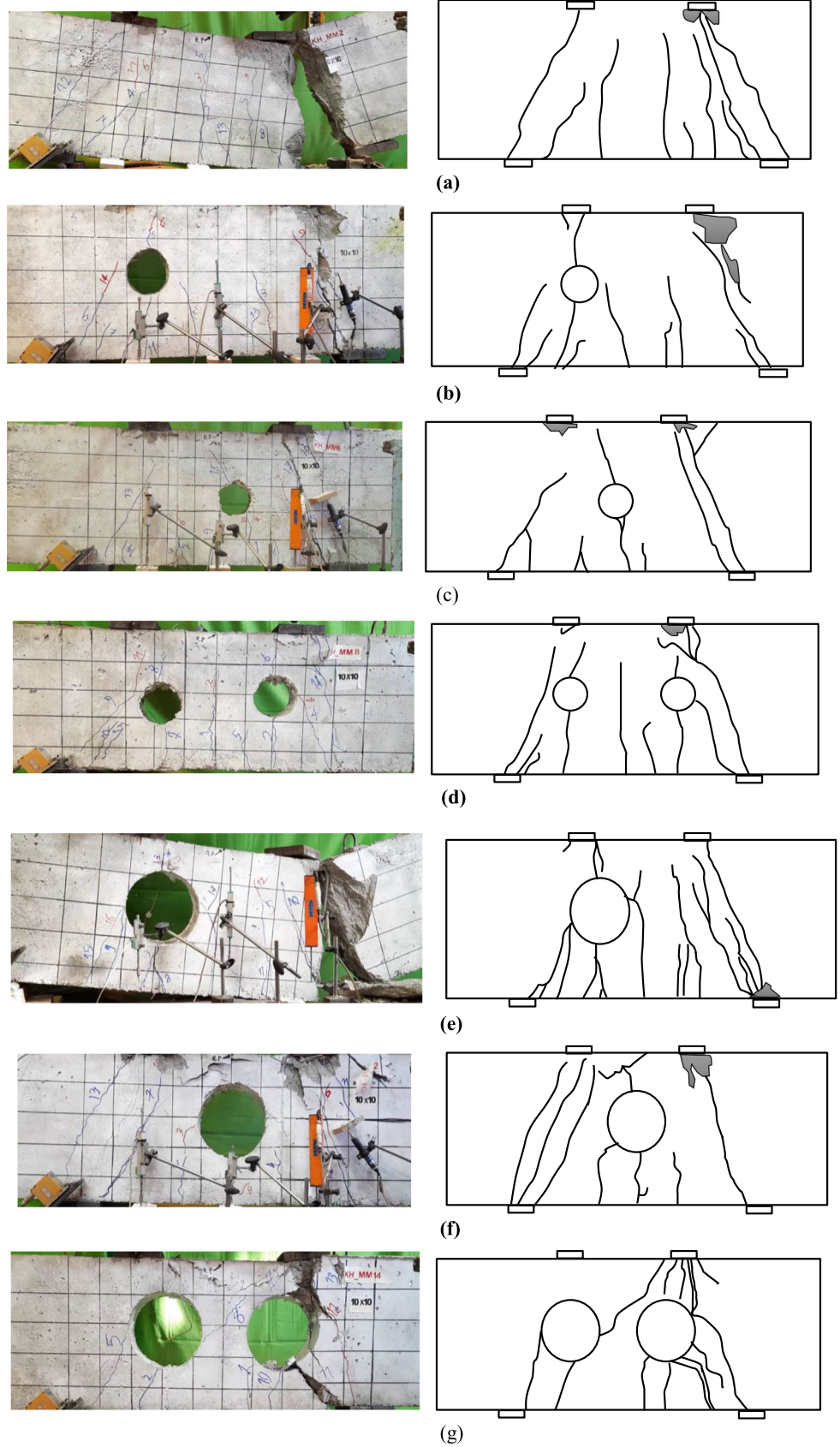
loading increased, a bending crack appeared at the mid-span of the beam. Gradually, the cracks at the top of the opening propagated towards the loading point. Ultimately, the beam failed with the collapse of the opening (Fig. 4e).

The initial crack in N11H1CD24 was flexural and occurred at the bottom of the opening and propagated into the opening. With an increase in loading, shear cracks formed in the lower part of the beam toward the loading point to the support area. A crack then formed at the top of the opening in line with the initial crack and propagated to the top of the beam. Gradually, cracks formed from the left and right sides of the beam. Ultimate failure of the beam occurred with the widening depth of shear cracks at the bottom of the opening (Fig. 4f).

The initial crack in N13H2L&RD24 was formed vertically at the mid-span of the beam. Afterwards, a shear crack was seen at the bottom of the left opening, and then the crack spread into the opening. Gradually, cracks formed along the load transfer axis above the left opening. As the load increased, shear cracks formed along each other on the right side of the beam, at the bottom and the top of the opening. The cracks on the left side propagated inside the opening and finally, the beam broke from the right side with the collapse of the opening (Fig. 4g).

In Group II, the initial crack in beam N2H0 formed with bending at the mid-span of the beam and extended to half the depth of the beam. Vertical cracks then formed at the bottom of the beam toward the loading point. Gradually, shear cracks formed on the sides of the beam. As loading increased, diagonal cracks formed on both sides of the beam. Failure of the beam occurred as the crack on the right side widened (Fig. 5a).

The initial crack in N4H1LD14 formed below the opening in shear and gradually extended into the opening. A crack also formed vertically at the mid-span of the beam towards the opening. Shear-bending cracks then formed on the right side of the beam. As loading increased, shear cracks formed along the axis of loading toward the support. Gradually, the cracks in the area of the strut on the right side of the beam widened. As the load increased, some of the concrete spalled at the loading point and on the right side of the beam. The beam ultimately failed with the widening depth of the diagonal cracks on the right side of the beam (Fig. 5b).

The initial crack in N6H1CD14 formed at the mid-span of the beam below the opening and extended towards the opening. As loading increased, shear cracks appeared on the right and left sides of the beam. Gradually, diagonal cracks formed along the axis of loading toward the support. Failure occurred as the crack on the right side of the beam widened (Fig. 5c).

The initial crack in N8H2L&RD14 formed at the mid-span of the beam. Gradually, vertical cracks formed under the opening on the right and extended into the opening. As the load increased, shear cracks formed on the right and left sides of the beam Ultimately, widening depth of the diagonal cracks on the right side of the sample caused failure of the beam (Fig. 5d).

The initial crack in N10H1LD24 formed after bending at the bottom of the beam and extended to half the height of the beam towards the opening. A shear crack gradually developed at the bottom of the opening and propagated into it. As the load increased, shear cracks formed on the right side of the beam. Ultimately, widening depth of the shear cracks on the right side caused failure of the beam (Fig. 5e).

The initial crack in N12H1CD24 formed in flexure at the bottom of the opening and propagated into the opening. As loading increased, bending cracks formed on the sides of the opening and propagated towards it. Gradually, diagonal cracks formed on the right and left sides of the beam. Before failure, some of the concrete spalled on the right and left sides of the beam and the specimen failed after widening depth of the shear crack on the right side (Fig. 5f).

The initial crack at N14H2L&RD24 formed vertically on the right side of the beam below the opening and propagated towards it. A vertical crack formed at the left side of the sample below the opening and propagated obliquely towards it. As loading increased, shear cracks appeared in the sample and cracks formed above the opening on the right side. Gradually, a diagonal crack formed on the right side. The beam failed as the crack widened and the opening collapsed on the right side (Fig. 5g).

In some samples, due to the symmetry resulting from the absence of openings or the placement of openings on the sides or in the middle of the beam, and considering the loading method, cracks initially appeared symmetrically in the samples. Over time, due to the propagation of cracks and the behavior of the concrete, the initial symmetry in the deformation of the samples is no longer observed. As shown in Figs. 4 and 5 symmetry is not evident in the samples at the moment of failure.

In the results for Groups I and II, the location of the opening in the axis of load transfer had an important effect on the type of rupture. In the beams of Group I, failure occurred after complete or partial collapse of the opening. In the beams of Group II, the openings usually remained intact even after failure of the beams.

3.3 Strain in Longitudinal Bottom Reinforcement (GFRP Bars)

To investigate the behavior of GFRP rebars in concrete samples, a strain gauge was installed at the mid-span of the longitudinal rebar in the tensile section of the beam. Determining the onset of strain on the GFRP rebars made it is possible to determine the onset of propagation of the main cracks in the samples. In all samples, loading in the GFRP
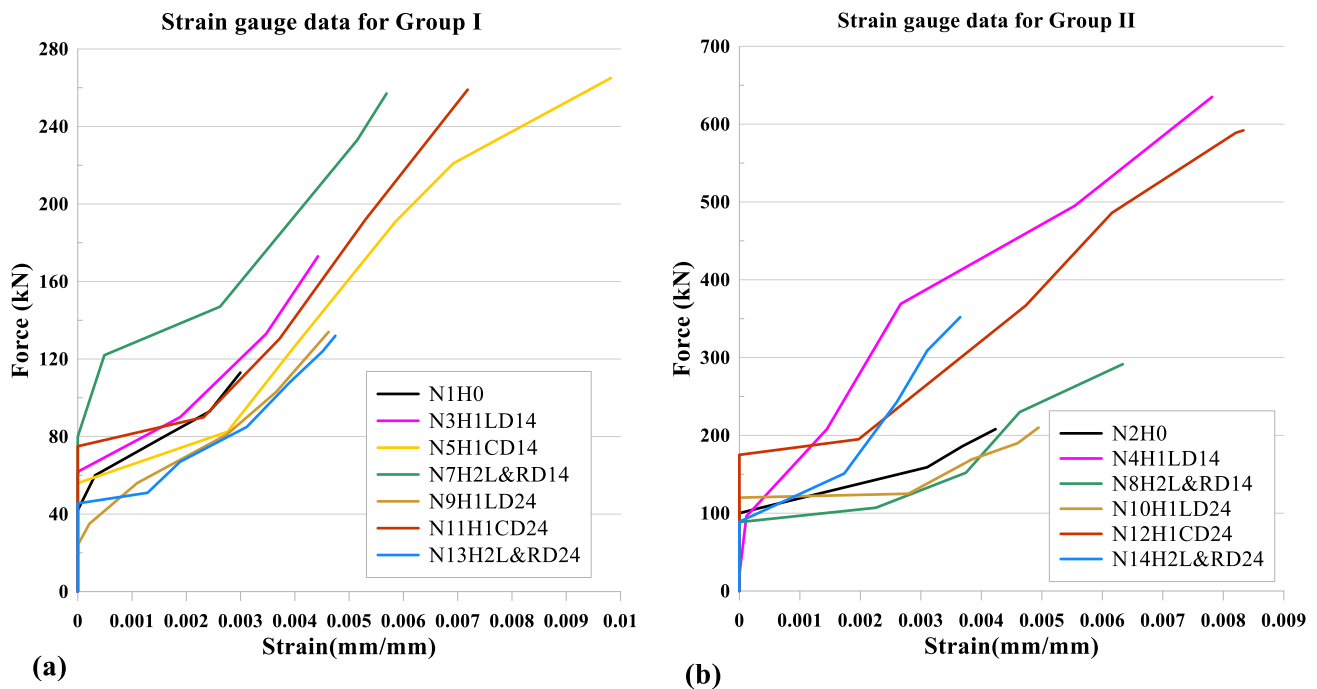
Fig. 6 Strain gauge data: **a** Group I; **b** Group II

rebars began after widening depth of the diagonal cracks. The result recorded by the strain gauges depended on the behavior of the GFRP rebars and their high tensile strength. The strain gauges either provided the results of rebar behavior up to the end of loading or were unavailable during loading and before the failure of the beam. Figure 6 shows changes in the slope of the graphs caused by development of cracks in the beam, a decrease in loading or in the load transfer path.

Adequate restraint along the length of the samples prevented separation of the GFRP rebars in the samples. Figure 7 shows the GFRP rebars failed because of load bearing. During testing of the samples, only the strain gauge on N6H1CD14 was unavailable and did not record information.

Loading of GFRP rebars in the beams of Group I began at lower loads than those of Group II. This related to the location of openings on the load transfer axis and rapid formation of primary cracks.

3.4 LVDT Results

Five LVDTs were installed on each sample to record the behavior of the beams during loading. LVDT1 and LVDT5 were installed obliquely to evaluate the behavior of the beam in the strut section on both sides of the beam. LVDT3 was installed at the mid-span of the lower part of the beam to record displacement of the mid-span. LVDT2 and LVDT4 were installed along the line of loading on the lower part of the beam to record the behavior of the beam. Figures 8 and 9 show the results from LVDT for Groups I and II.

By comparing the results of Figs. 8 and 9, it can be seen that the largest change interval in the relative displacement parameter is related to the control sample of Group I N1H0, which ranges from -18 to + 18, while in the similar sample in Group II (N2H0) these changes are in the range of -8 to + 8. The force-lvdt diagrams are symmetrical in both N1H0 and N2H0 samples, and the corresponding values of LVDT1 and LVDT5 match. By checking the graphs, it is clear that the symmetry of the graph is changed by creating an opening, and the values related to LVDT1 and LVDT5 are separated from each other. In all samples in two groups, the graph related to LVDT3 is located on the right side, and the reason for this is the location of this LVDT in the center and at the bottom of the beam opening. Except for N14H2L&RD14 and N14H2L&RD24 samples, in all samples, the diagram related to LVDT4 is on the left side. This issue is due to the failure of the mentioned samples and the failure of the opening on the right side of the beam at the moment of breakage.

According to Fig. 9, it can be seen that in Group II beams, creating a small scale opening in the middle of the span compared to the control beam, causes insignificant changes in the force-lvdt diagram, while according to Fig. 8, this is the case for Group I beams. By comparing the diagram of N5H1CD14 beam compared to N1H0 beam, it is shown that the numerical range related to relative displacement has decreased and the numerical range related to force has increased.
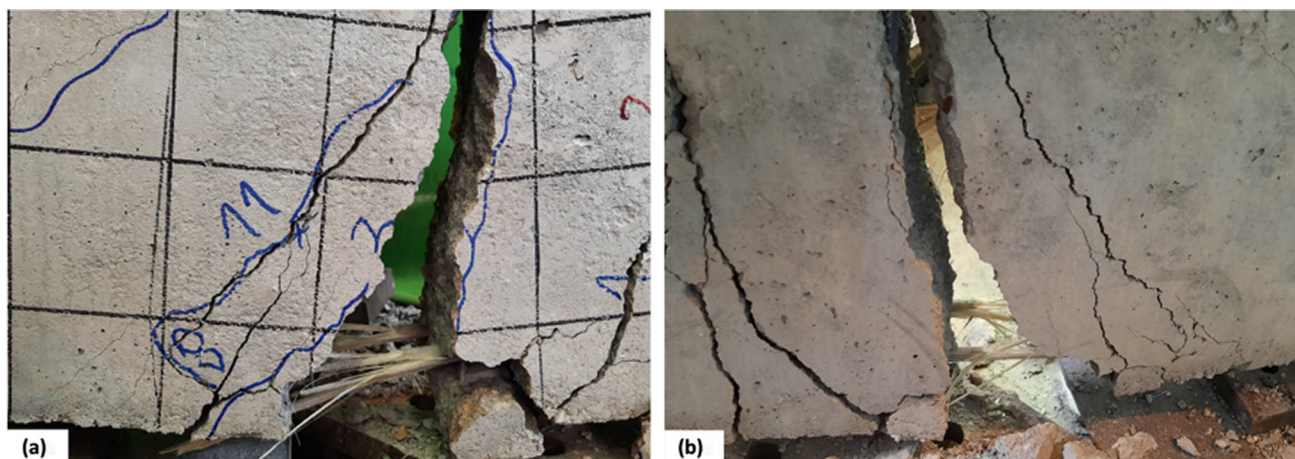
Fig. 7 Failure of GFRP rebar: **a** front view; **b** back view

3.5 Load–Deflection Response

The applied load and the mid-span deflection were recorded for each beam and then were plotted as load versus mid-span deflection curves (Fig. 10). It is evident that Group II endured greater ultimate loads than Group I for beams with and without openings. It could be concluded that resistance in the beams increased with a decrease in a/d.

The location of the openings in the beams of Group I affected the load transfer path to the support more than did the openings in Group II. This was related to an increase in the diameter of the opening and the number of openings and caused a decrease in the ultimate strength of the beams. The presence of an opening at the mid-span of the beam had no effect in reducing the resistance of the beam and even increased the ultimate resistance compared to the case without an opening. An increase in the diameter of the opening caused loading of the GFRP rebars to occur faster than in the case without an opening or with an opening of 14 cm in diameter. This has been observed in studies on steel rebars [10].

For the samples in Group I with openings of 14 cm in diameter, a relatively small diameter, all four graphs showed a similar trend. These openings did not significantly reduce the initial stiffness of the beam. The graphs of N1H0 and N5H1CD14 were nearly identical. N5H1CD14 had endured more ultimate force, however, the displacement at the mid-span of the beam in these two samples was similar because of the relatively small diameter of the opening and the presence of reinforcements around the opening. As expected, the line of the graph for N7H2L&RD14 was lower than for N3H1LD14 because of the increase in the number of openings and the decrease in the load transfer path.

The test results showed that the line in the force–displacement diagram for N11H1CD24 was higher than for beams N1H0 and N5H1CD14 because the size of the opening, the decrease in the tensile and compressive levels of the concrete and the increase in the resistant arm of the section. With an increase in the diameter of the opening, N9H1LD24 showed less resistance than N3H1LD14. The least resistance was for N13H2L&RD24 because of the number and diameter of the openings.

Analysis of the results of Group II showed that the beams with openings were farther from the load transfer axis compared to Group I, the amount of ultimate loading tolerated was higher. The trends of N2H0 and N6H1CD14 were similar at the beginning, but displacement of the mid-span of N2H0 was less than of N6H1CD14 although loading was the same in both samples. N8H2L&RD14 showed less resistance and mid-span displacement than did N4H1LD14. This likely related to the increase in the number of openings, which decreased the beam stiffness.

The test results showed that the force–displacement line for N12H1CD24 was higher than for the N2H0 and N6H1CD14 and the ultimate resistance and mid-span displacement were less. Because of the larger opening diameter, N10H1LD24 showed less resistance than N4H1LD14. The least resistance in Group II was recorded by N14H2L&RD24 and related to the number and diameter of the openings. In Fig. 10, the force caused by formation of the initial crack is denoted as a hollow circle. The graphs in Fig. 10a can be equivalently represented as two overall trends. Based on this, the behavior of the beams can be categorized into two ranges: elastic and non-elastic. This is not observed in the graphs in Fig. 10b, where it seems that the overall trend of the graphs does not change from the beginning to the end of the sample failures. The reason for this may be related to the location of the openings and the influence of the openings on the failure process of the beams. As indicated by the failure modes of the beams, in Group II, the openings remain visibly intact until the end of loading, while in similar samples in Group I, the openings are damaged. The primary reason
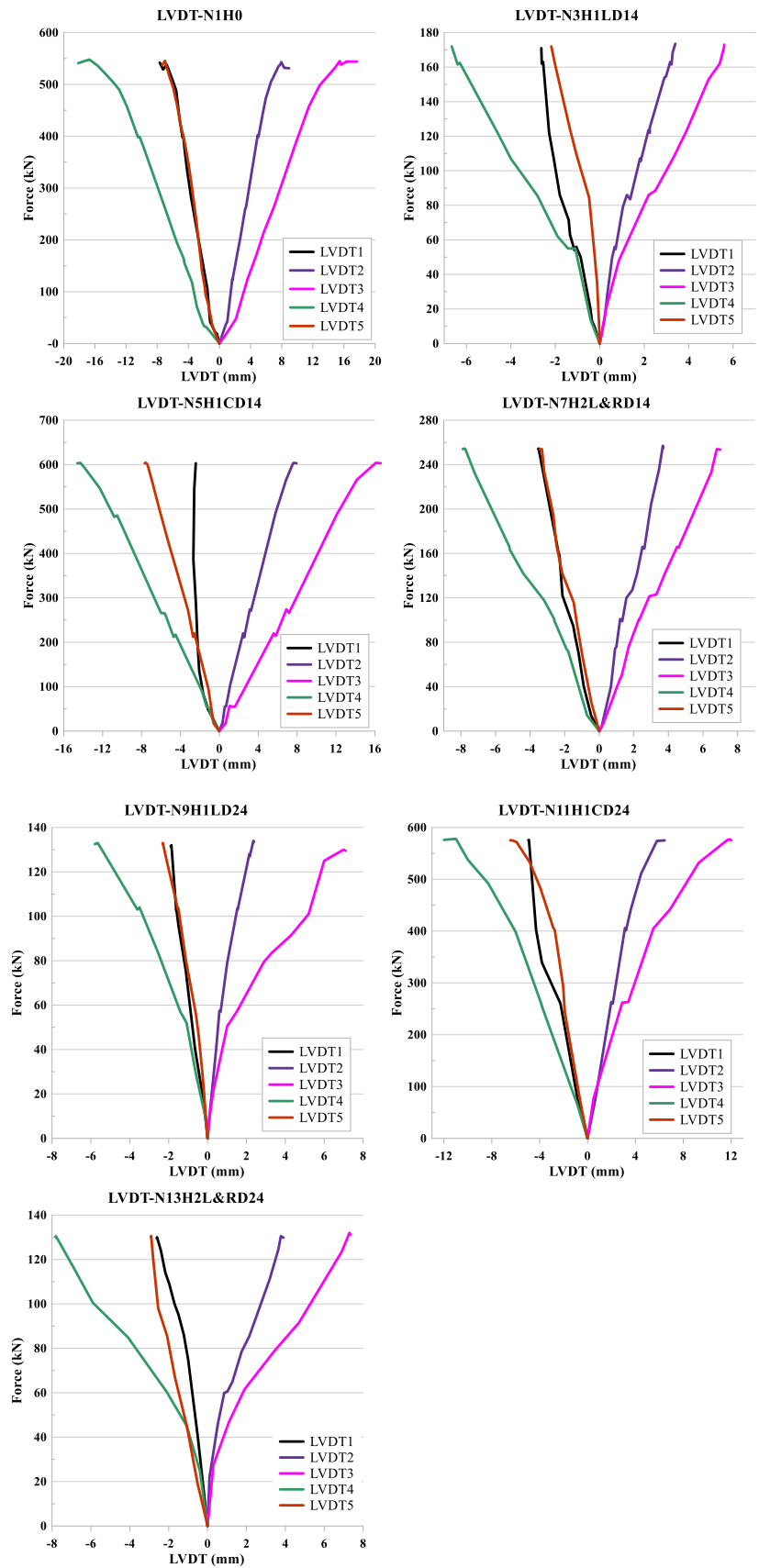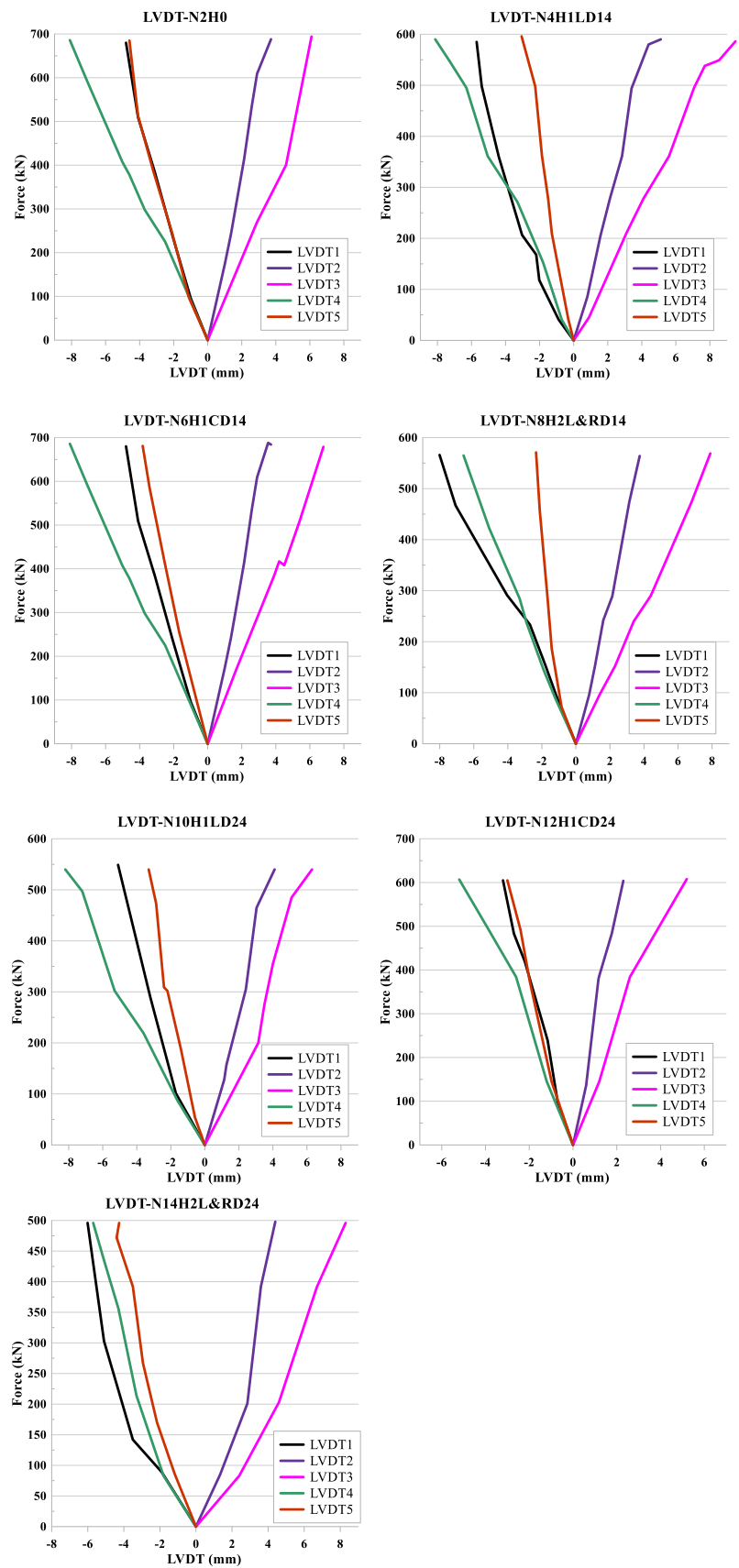
Fig. 8 LVDT results for Group I
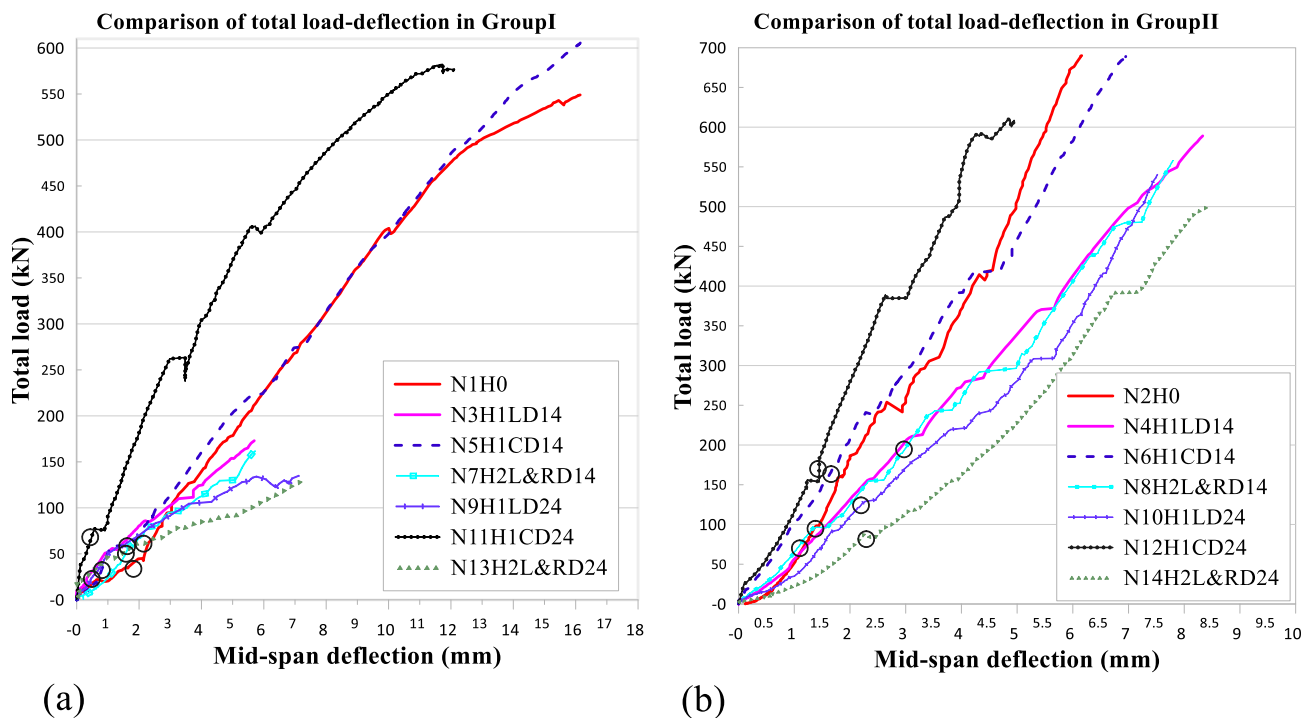
Fig. 9 LVDT results for Group II

Fig. 10 Comparison of total load–deflection: **a** Group I; **b** Group II

for the failure of the beams is the destruction of the openings and the propagation of cracks in their vicinity. The results clearly indicate that the behavior of the beams in Group II has less ductility compared to Group I. Despite having greater strength under higher loads, their deformation is less than that of similar specimens in Group I. Additionally, their failure is more brittle and sudden compared to the beams in Group I.

4 Discussion

The test results and the effects of the size, number and locations of the openings and the shear span-to-depth ratio on the behavior of the beams is discussed in this section.

4.1 Effect of a/d Ratio

One of the most important parameters in determining the behavior of deep beams is the shear span-to-depth ratio (*a/d*). The results of research has shown that an increase in *a/d* will decrease the ultimate strength of beams. In the STM, the load is transferred to the supports by means of the struts and ties. With an increase in *a/d*, the angle of formation of the struts decreased from vertical to oblique. The effect of bending on the struts caused a decrease in the ultimate capacity of the beams. This also affected the failure mode of the beams such

that, with an increase in *a/d*, the failure mode changed from shear to shear and flexural shear.

Other factors affecting the failure mode of beams, such as the size, number and location of openings, have been discussed in Sects. 4.1 to 4.3. In this section, each sample in Group I was compared with the corresponding sample in Group II to determine their ultimate capacity, ultimate displacement, the energy absorbed and the failure mode based on the effect of *a/d*. Figure 11 shows the ultimate capacity and ultimate deflection of the beams.

From the results for beams without openings, it is clear that the ultimate capacity of N1H0 was 19% lower than for N2H0. Comparison of the results for two samples with openings with diameters of 14 cm on the left side of the beam, it was determined that the ultimate capacity of N3H1LD14 was 70% less than of N4H1LD14. Comparison of samples with similarly sized openings at the mid-span of the beam revealed that the ultimate capacity of N5H1CD14 was 11% lower than of N6H1CD14. Comparison of beams with two openings with diameters of 14 cm revealed that the ultimate capacity of N7H2L&RD14 was 71% lower than of N8H2L&RD14.

Comparison of the results of two samples with a 24-cm in diameter opening on the left side of the beam revealed that the ultimate strength of N9H1LD24 was 75% lower than of N10H1LD24. The results of two beams with 24-cm diameter openings at their mid-spans showed that the ultimate capacity of N11H1CD24 was 5% lower than of N12H1CD24.
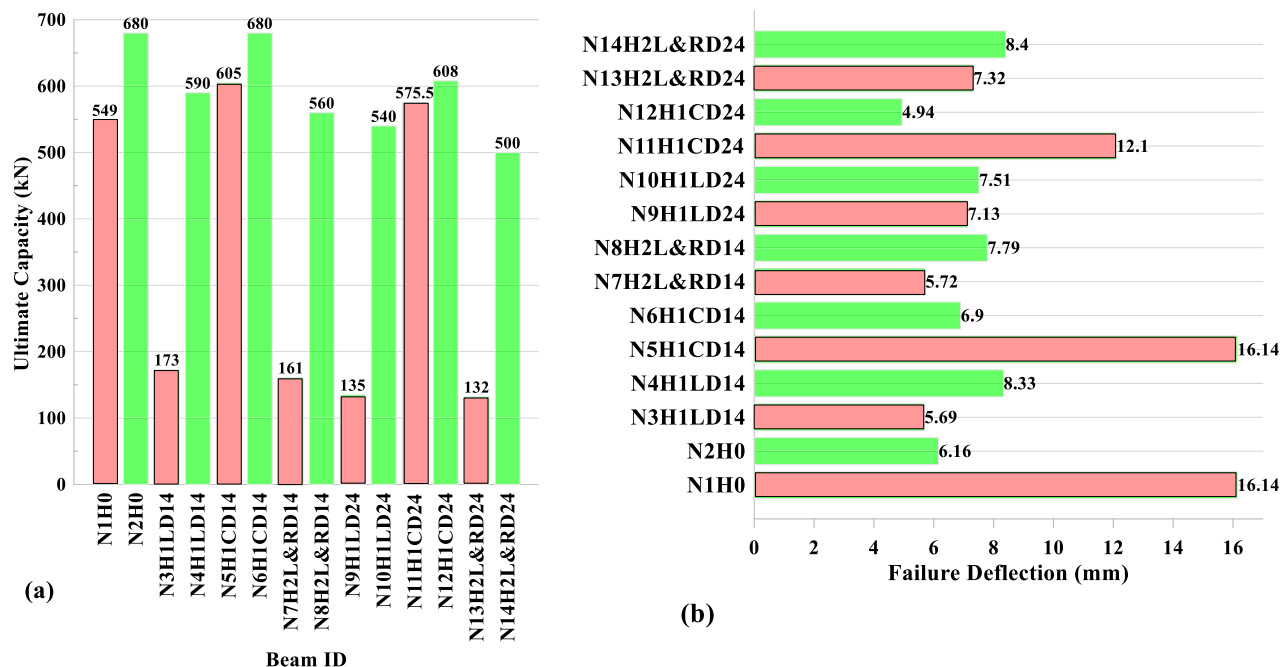
Fig. 11 Behavior of specimens: **a** ultimate capacity; **b** failure deflection

Comparison of the results of the beams with two 24-cm diameter openings showed that the ultimate capacity of N13H2L&RD24 was 73% lower than of N14H2L&RD24.

The ductility of the samples was determined by calculating the energy absorbed by each beam was calculated at failure. For this purpose, the area under the force–displacement diagram of each beam was calculated. Figure 12 allows comparison of the results for the amount of energy absorption by each sample.

It is evident that beams N2H0, N6H1CD14 and N12H1CD24 recorded 66%, 54% and 64% less energy absorption than N1H0, N5H1CD14 and N11H1CD24, respectively. Despite the greater ultimate capacity beams in Group II, the reason for the decrease in energy absorption was the greater displacement in Group I compared to the corresponding samples in Group II. This indicates that, for beams without an opening or with an opening at the mid-span, an increase in *a/d* caused a decrease in energy absorption and brittle behavior of the beam.

It was found that the amount of energy absorption by other specimens in Group II was higher than the corresponding beams in Group I. This was the result of the greater final displacement and ultimate capacity of the beams. The amount of energy absorption in N3H1LD14, N7H2L&RD14, N9H1LD24 and N13H2L&RD24 was 76, 76, 69 and 67% lower than in N4H1LD14, N8H2L&RD14, N10H1LD24 and N14H2L&RD24, respectively.
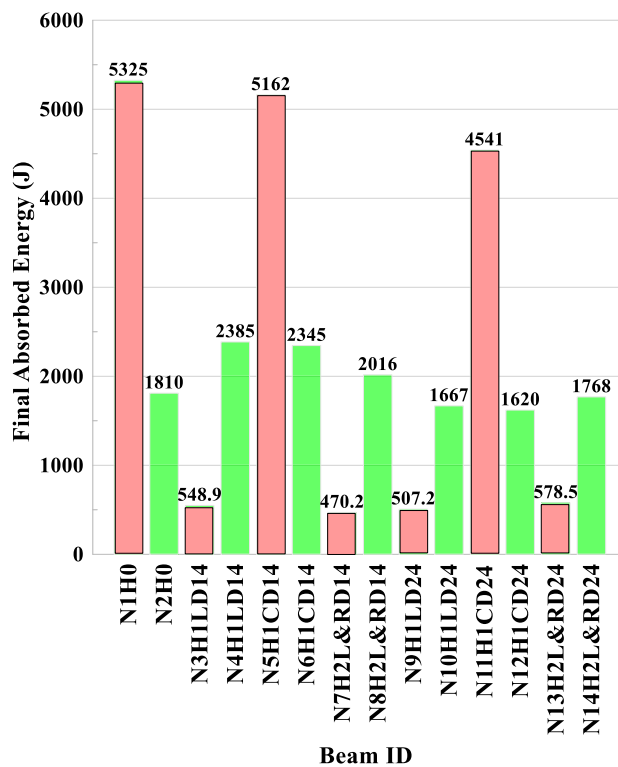

Fig. 12 Ultimate absorbed energy

4.2 Effect of Opening Location

The location of the opening had a significant effect on the failure mode and the ultimate strength of the beams. The results of Group I show that the location of the opening in the shear zone caused a decrease the ultimate strength of the beams. The ultimate resistance of N3H1LD14 and N9H1LD24 decreased by 68% and 75%, respectively, compared to N1H0. The location of the opening at the mid-span of the beam had a positive effect on the behavior of the beams. The ultimate strength of N5H1CD14 and N11H1CD24 increased by 10 and 4%, respectively, compared to N1H0.

The creation of an opening in the shear zone of Group II reduced the ultimate strength of N4H1LD14 and N10H1LD24 by 13 and 20%, respectively, compared to N2H0. Unlike Group I, the location of the opening at the mid-span of the beams did not increase their ultimate strength. The ultimate strength of N6H1CD14 was equal to that of N2H0, but the ultimate strength of N12H1CD24 decreased by 10%.

In Group I, the failure mode of N1H0 was combined shear and flexural shear. The location of the openings between the loading point and the support altered their failure modes. In N3H1LD14 and N9H1LD24, the failure mode was only shear. In N5H1CD14, like the control beam without an opening, the failure mode was combined shear and flexural shear and in N11H1CD24 was flexural shear. In Group II, the beams with an opening on the left side, because the opening was located outside the area of the load transfer to the support, it had no effect on the failure mode of the beams. The failure modes of N4H1LD14 and N10H1LD24 were shear, like N2H0. In these beams, rupture occurred from the right side of the beam (where there was no opening) and none of the openings were seriously damaged. The failure mode in N6H1CD14 and N12H1CD24 was shear. The results showed that as the distance of the opening from the area of load transfer to the support increased, the effects of the presence of an opening on the behavior of the beam decreased.

4.3 Effect of Opening Diameter

Increasing the cross-sectional area of the openings reduced the stiffness of the beams and their ultimate capacity. The results of Group I show that an increase in the diameter of the opening from 14 to 24 cm decreased the ultimate capacities of N9H1LD24, N11H1CD24 and N13H2L&RD24 by 21, 4 and 18% compared to N3H1LD14, N5H1CD14 and N7H2L&RD14, respectively. In Group II, an increase in the opening diameter from 14 to 24 cm decreased the ultimate capacities of N10H1LD24, N12H1CD24 and N14H2L&RD24 by 8, 10 and 10%, respectively compared to N4H1LD14, N6H1CD14 and N8H2L&RD14, respectively.

The effects of the load transfer path to the supports with an increase in the cross-section of the opening can also affect the failure mode. For example, in Group I, the failure mode of N5H1CD14 was shear and flexural shear. With an increase in the diameter of the opening in N11H1CD24, the failure mode changed to flexural shear. In Group II, an increase in the cross-section area of the opening had no effect on the failure mode.

As it is clear from the results, the changes in the reduction of the final strength of the beams due to the increase in the opening diameter are more in the samples of Group I than in Group II. This issue is also effective regarding the way the beams break. In beams of Group I, with the increase in the diameter of the opening, the expansion of cracks and final rupture in the beams in the area of the openings is evident, while in all the beams of Group II, except N14H2L&RD24, the openings are not seriously damaged until the end of loading.

4.4 Effect of Opening Number

As the number of openings increased, the stiffness of the beams decreased. In the results of Group I, an increase in the number of openings from 1 to 2 decreased the resistance of N7H2L&RD14 and N13H2L&RD24 by 6 and 2%, respectively, compared to N3H1LD14 and N9H1LD24, respectively. In Group II, an increase in the number of openings caused decreases in the ultimate strengths of N8H2L&RD14 and N14H2L&RD24 of 5 and 7%, respectively, compared to N4H1LD14 and N10H1LD24, respectively.

The effect of a decrease in the load bearing capacity of the beams caused by an increase in the number of openings was less than the effect of changes in diameter and location of the openings. Increasing the number of openings, which influenced the path of load transfer to the supports, could affect the failure mode of the beam. In Group I, N7H2L&RD14 and N13H2L&RD24 failed in shear with an increase the number of openings. In Group II, N8H2L&RD14 experienced shear failure and N14H2L&RD24 experienced shear and flexural shear failure.

Considering the location of the openings in the area of the load transfer axis to the support in Group I, the increase in the number of openings has not caused a change in the failure mode of the beam, and the final rupture of the beams occurs due to the loss of the openings. This is despite the fact that in Group II, except N14H2L&RD24, all openings are not seriously damaged until the beam breaks.

5 Comparison of Test Results with STM Results

Since the 1960s, various empirical and analytical approaches have been proposed to evaluate the shear capacity of RC deep beams [41]. The application of stress fields to the RC design
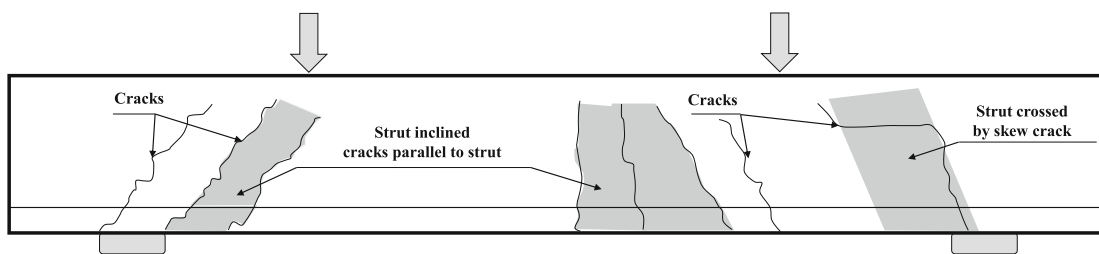
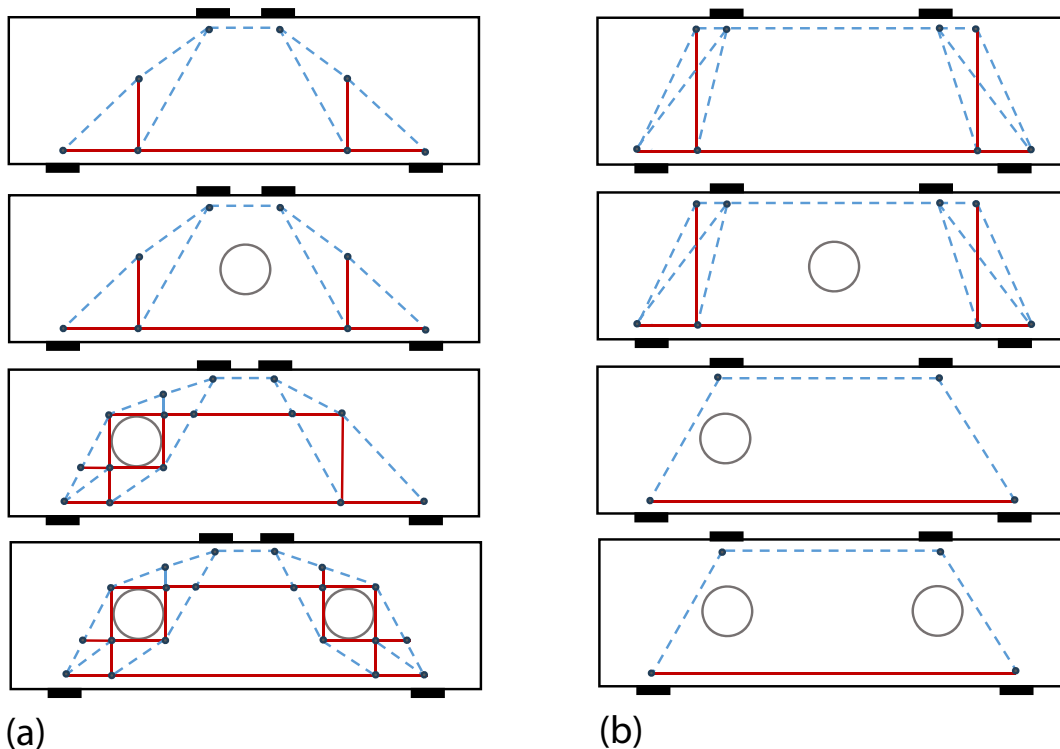**Fig. 13** Strut recognition from cracks created in beam

(a)   (b)

Fig. 14 STM components for samples in: **a** Group I; **b** Group II

based the lower-bound theorem of limit analysis is a more recent development and represents an important advance in RC [42, 43]. The STM is based on the lower-bound plasticity theorem and is strictly an equilibrium model in which the stresses are calculated by satisfying the equilibrium and yield criteria while neglecting the compatibility condition. Engineers also can choose the efficiency of the STM that satisfies the equilibrium condition [44, 45]. Similar to a real truss, the STM uses of compression struts and tension ties interconnected at nodes. The STM could fail in one of the following modes:

- The tension tie could yield or the anchorage of the ties could fail.
- One of the struts could be crushed as the stress in the strut exceeds the effective compressive strength of the concrete.

- A nodal zone could fail under stresses greater than the effective compressive strength of the concrete [42].

The nonlinear material properties of concrete and steel are considered in the calculations for shear capacity of deep beams in the STM. The STM is utilized for the design of reinforced deep beams and accounts for the beneficial effect of arch action on shear capacity in reinforced concrete members. Additionally, a shear plastic hinge model has been developed to analyze the nonlinear shear behavior of deep reinforced concrete members, considering the contributions of web concrete, transverse reinforcement, and inclined concrete compression chord to the shear response.

The present study used composite rebars; thus, yielding did not occur in the tensile part of the beam and failure occurred because of breakage of the longitudinal rebars.

The data on the restraining length indicated that all GFRP rebars carried the load up to the moment of failure. For any given structure, several STMs would be possible. Figure 13 shows ways to detect the strut using cracks that occur in a sample.

The STM components for the samples were developed using the dimensions of the openings and their placement in the beams In Fig. 14, the red lines denote the tensile members (tie), the blue dashed lines denote the compression members (strut) and solid circles denote the nodes.

According to the dimensions, shape and location of the opening in the deep beams, which may cause the interruption of the return transmission path, the way of forming the STM components are changed. If the openings are not located near the axis of load transfer to the support or their dimensions are very small, the formation of STM components are the same as if there is no opening, but if the opening is such that the path of load transfer cut off, tie, strut and nodes are redistributed around the opening and create different states according to the type of opening, its dimensions and placement. Inherently, the load is transferred to the support by the shortest possible path.

In the STM, the provisions of the American code did not account for the shear strength of RC deep beams reinforced with FRP rebars. Canadian code S806-2012 [46] used the equations developed for steel-RC deep beams from CSA A23.3–04 [47] for beams reinforced with FRP bars. The Canadian code also considers the effect of FRP bars through the effectiveness factor, which depends on the shear span-to-depth ratio and strain in the longitudinal FRP bars. Table 4 compares the experimental results and the predictions of the provisions from the American [31] and Canadian [46] code provisions.

The STM recommended by ACI 318–19 Code [31] resulted in predicted capacities close to those achieved experimentally with an average experiment-to-predicted value of 1.15 and COV of 10.8%. The STM recommended by the Canadian code S806-2012 [46] accounts for the effect of different reinforcement materials by considering the strain on the longitudinal reinforcement when calculating the strut resistance. The resultant predictions for GFRP-reinforced deep beams were, however, found to be conservative, with an average of 1.8 and COV of 10.9%.

The predicted results calculated by the American and Canadian regulations are conservative compared to the laboratory results, however, the values calculated by the American regulation are more accurate than the Canadian regulation, the reason for this can be found in the correction coefficients included in the relations for calculating the shear capacity of deep beams and the latest edition of the American regulation.

Figure 15 shows the distribution of the calculated data based on the regulations and test results. As expected, the

Table 4 Experimental results vs. predictions of ACI 318–19 and S806-2012 codes

Group	Specimen	P_U(kN)		
		EXP	$\frac{EXP}{ACI}$	$\frac{EXP}{CSA}$
Group I	N1H0	549	1.1	1.7
	N3H1LD14	173	1.25	1.9
	N5H1CD14	605	1.3	1.5
	N7H2L&RD14	161	0.95	2
	N9H1LD24	135	1.15	1.8
	N11H1CD24	575.5	1.4	2.2
	N13H2L&RD24	132	1.2	1.9
Group II	N2H0	680	1.05	1.6
	N4H1LD14	590	1.15	1.8
	N6H1CD14	680	1.3	1.5
	N8H2L&RD14	560	0.98	2
	N10H1LD24	540	1.05	1.6
	N12H1CD24	608	1.25	1.9
	N14H2L&RD24	500	1.1	1.8
	Mean		1.15	1.8
	SD%		12.6	19.6
	COV%		10.8	10.9

resistance calculated by the STM was conservative and, except for one case, the laboratory values were higher than it. As it is clear in the Fig. 15, the results calculated by each regulation have a proper correlation and have a clear trend. At low capacities in the range of 100 to 200 kN, the correlation between the data is higher. All the data, except one of them, are above the 45 degree line, which indicates the conservativeness of the STM method. Among the data, the results related to the Canadian regulations are conservative and less than the American regulations.

6 Numerical Modeling

In the present study, the nonlinear finite element (F.E.) method utilizing ABAQUS software environment is used in order to simulate the simply supported RC deep beams with and without openings.

6.1 Materials Properties

The specifications used in ABAQUS modeling include concrete, steel and GFRP composite materials. As it is known, GFRP materials have a completely linear and elastic behavior unlike steel, and this point has been carefully defined in the definition of material characteristics. For conducting a linear
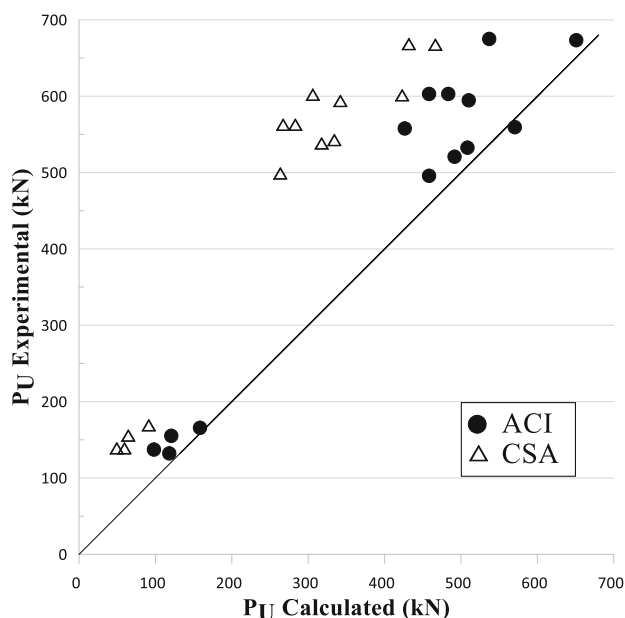
Fig. 15 Distribution of calculated data based on regulations and test results

Table 5 Characteristics of concrete

Item	$f_c^{'}$ (Mpa)	f_t (Mpa)	f_r (Mpa)	E_c (Mpa)	υ
Value	29	3.1	3.5	24,667	0.2

Table 6 Plastic parameter of the CDP model

Parameter	Value
Dilation angle	36
Eccentricity	0.1
Ratio of initial biaxial compressive strength to initial compressive strength	1.16
Shape factor for yield surface	0.67
Viscosity parameter	0.001

analysis, it is necessary to define at least two fundamental linear material properties: Young's modulus (E) and Poisson's ratio (υ). These parameters describe the linear elastic behavior of the material. On the other hand, for a nonlinear analysis, the uniaxial behavior of the steel and concrete materials should be determined beyond the elastic range. This allows simulating the performance of these materials at high strain levels, where their response becomes nonlinear [48, 49]. For modeling the concrete material behavior, several constitutive models have been proposed [50, 51], such as Drucker-Prager [52], Ottosen [53], and Willam-Warnke [54]. However, the concrete damage plasticity model (CDP) is among the most preferred approaches. This model can effectively reflect the degradation in concrete strength and stiffness by incorporating tension and compression damage parameters [55, 56]. There are primarily two material modeling approaches for concrete in ABAQUS: the concrete smeared cracking model and CDP model [57, 58]. Many researchers [59–61] have utilized the CDP model in simulating various structural elements made of reinforced concrete. These studies have found that the CDP model can accurately capture the real-world behavior of the tested reinforced concrete members. The model's ability to account for both the damage and plastic deformation mechanisms in concrete makes it a versatile and reliable tool for nonlinear analysis of concrete structures. In present research, CDP model is used for concrete modeling. In Table 5 the characteristics of concrete including compressive strength($f_c^{'}$), concrete tensile strength (f_t), rupture stress(f_r), Modulus of elasticity(E_c), and Poisson's

ratio (υ) considered in the modeling of the samples are presented.

Various equations have been presented by researchers to describe the stress–strain behavior of concrete under uniaxial loads [62–64]. Hognestad model [65] has been used in this study. To define the plastic behavior in the CDP model, five plastic constants and two sets of stress–strain relationships for compression and tension are required [66–68]. These parameters are tabulated in Table 6.

GFRP rebars were simulated as elastic isotropic one-dimensional material until failure [69]. The stirrups material was modeled using an elastic-perfectly plastic stress–strain relationship [6]. The steel bearing plates and support plates were represented as linear isotropic materials. Considering the rigid behavior of these plates, its modulus of elasticity was considered 100 times higher than that of steel.

6.2 Load and Boundary Conditions

A steel plate segment measuring 150 mm × 150 mm × 20 mm was used and placed on top of the beam at a two-point load. Additionally, steel plates of the same dimensions (150 mm × 150 mm × 20 mm) were positioned at the left and right rigid support sides of the specimens. This was done in order to simulate the experimental loading setup and boundary conditions as accurately as possible in the F.E. modeling. The perfect bond between the beam element and plate surface was assumed based on the tie constraint. The Conditions of the pin support that allow rotation in only one direction with a supply restraint to the lateral displacement was applied on the right side [70]. The roller condition, which allows the beam to rotate freely in both the lateral and vertical directions, was applied on the left side. Two reference points were created at the center of each rigid plate. These reference points were used to apply a load and were connected to the beam
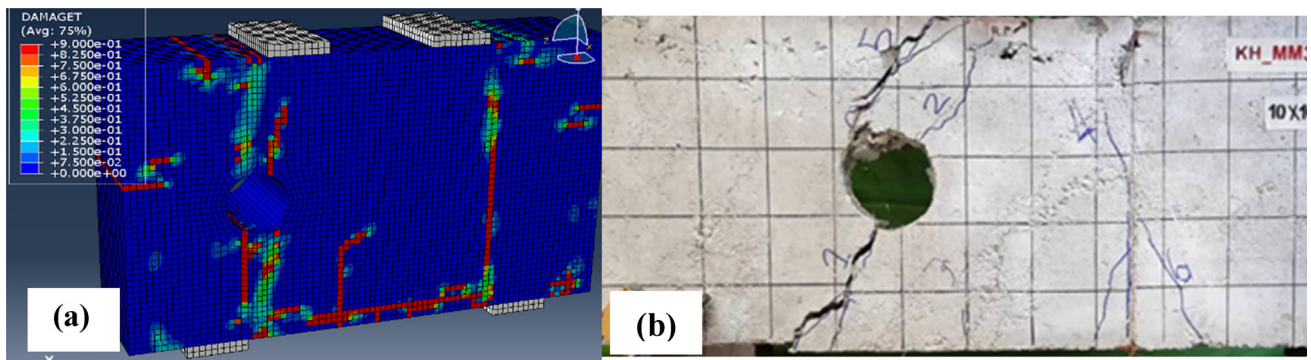
Fig. 16 Failure mode of N3H1LD14: **a** F.E. modeling; **b** experiment

Table 7 Comparison of experimental and F.E. model results

Group	Specimen	Failure load (kN)			Failure deflection (mm)		
		EXP	F.E. model	Percentage Difference $[(\frac{EXP}{F.E.model}) - 1]$ (%)	EXP	F.E. model	Percentage Difference $[(\frac{EXP}{F.E.model}) - 1]$ (%)
Group I	N1H0	549	540.2	1.62	16.14	15.2	6.18
	N3H1LD14	173	178	−2.8	6.16	6	2.6
	N5H1CD14	605	589.3	2.6	6.69	6.05	10.57
	N7H2L&RD14	161	165.3	−2.6	8.33	9.1	−8.46
	N9H1LD24	135	130.4	3.5	16.14	15.7	2.8
	N11H1CD24	575.5	565.2	1.8	6.9	6.2	11.2
	N13H2L&RD24	132	139.5	−5.3	6.72	6.08	10.5
Group II	N2H0	680	664.8	2.2	7.79	8.1	−3.8
	N4H1LD14	590	596.7	−1.1	7.13	7.62	−6.4
	N6H1CD14	680	665.8	2.13	7.51	7.1	5.7
	N8H2L&RD14	560	570.3	−1.8	12.1	11.9	1.6
	N10H1LD24	540	548.1	−1.4	4.94	5.1	−3.13
	N12H1CD24	608	624	−2.56	7.32	6.98	4.87
	N14H2L&RD24	500	508.1	−1.59	8.4	9	−6.67

through the coupling constraints employed in ABAQUS. The load was applied using a displacement control method, which allowed for the implementation of a smooth step amplitude [71].

6.3 Element Type and Mesh

A three-dimensional (3D) F.E. model was generated to simulate an RC deep beam that is strengthened with a GFRP and steel bars and has a circular web opening. The modeled components include concrete beams, GFRP bars, shear stirrups, and a load-spreading steel plate section. A solid brick element (C3D8R) was used to model the concrete and fill materials. This element type has three degrees of freedom per node and reduced integration, which allows it to capture the complex non-linear behavior, cracking, and plastic deformation in three orthogonal directions under both monotonic and cyclic loading conditions [72]. The spreader load and support reaction plates were defined using solid elements (C3D8R) [73, 74]. The longitudinal GFRP bars were modeled as truss elements (T3D2) that have three translational degrees of freedom at each node [75]. The approximate global size of the mesh elements ranged between 40 and 40 mm. The concrete beam and steel plate were discretized using a hexahedral solid element with eight nodes, and a refined mesh was applied around the circular opening.

6.4 Numerical Result

The numerical analysis results for all specimens have been compared with the results obtained from the tested beams. The findings of the predicted F.E. modeling and the experimental results are summarized in Table 7. Low percentage differences demonstrate that numerical results are verified.

Figure 15 depicts the predicted F.E. model result for the failure process based on the observed crack patterns (N3H1LD14). Results for other specimens are not included here for brevity. According to the CDP model, the principal plastic strain (PE) provides the clearest visualization of the crack patterns in Abaqus, particularly through the maximum PE [73]. Figure 16 indicates that the developed F.E. model closely resembles the failure process observed experimentally, which confirms the specific capability and power of the CDP model in accurately predicting the crack pattern in the concrete element at the onset of failure.

In a number of specimens, the results exceed the laboratory findings, while in others, they fall short. Another factor contributing to the discrepancy between laboratory and numerical results is the loading procedure of the deep beams in the laboratory. Occasionally, the loading element may be positioned directly on the vertical shear reinforcement, creating conditions that differ from initial assumptions. This can lead to slightly higher experimental results than the true values. Ultimately, given the small differences and the close alignment of the numerical and experimental results, it can be concluded that the laboratory findings have been validated by the numerical modeling.

7 Conclusions

The current study investigated the behavior of deep RC beams with and without openings with GFRP longitudinal bars and steel transverse bars. For this purpose, 14 beams were subjected to four-point bending up to the moment of failure. The ratio of the shear depth to effective height of the beam, as well as the dimensions, number and location of the openings were considered as variables. The most important results of this research are as follows:

1. The initial crack in each sample formed by bending or shearing. In all samples, failure occurred due to widening depth of the shear cracks and by shearing.
2. Comparison of the results with those of other research determined that the onset of loading for the GFRP tensile bars occurred at a lower load than for the steel bars. This resulted from the formation of cracks in the tensile part of the beam. After examination of all samples and determination of how the GFRP rebars failed, because no separation was detected in any of the samples, it is

considered appropriate to consider a restraint length of 30 cm.
3. The samples are divided into two groups depending on the shear depth to effective height of the beam (a/d). In Group I, $a/d = 0.9$ and, in Group II, $a/d = 0.5$. Comparison of the samples of the both groups revealed that the ultimate capacity of the specimens decreased with an increase in a/d from 0.5 to 0.9.
4. The results revealed that the initial slope of the force–displacement diagrams for beams with an opening of 14 cm in diameter were similar. This indicates that, with the placement of a small opening with transverse reinforcements around it, the effect of the opening on the stiffness of the beams can be reduced to near the initial values in the diagram. This does not apply to beams with openings of 24 cm in diameter.
5. Assuming that the dimensions of the openings in the beams of each group were held constant, the location and number of the openings had direct effects on the ultimate load borne by the beams. Beams with two openings on the left side had lower ultimate loads because of the decrease in the larger part of the load transfer path compared to the single-opening beams. The location of the openings at the mid-span of the opening increased the amount of the ultimate loading borne by the beam.
6. Comparison of the laboratory results and those of the STM in the ACI 318–2019 and S806-2012 codes determined that the STM was conservative and the ultimate capacity of the beams using this method was lower than the corresponding laboratory values.
7. Finite element modeling was performed to confirm the numerical accuracy of the samples, and a strong correlation was found between the numerical and laboratory results.

Declarations

References

1. Li, R.; Deng, M.; Zhang, Y.; Wei, D.: Shear strengthening of RC deep beams with highly ductile fiber-RC jacket. J. Build. Eng. **48**, 103957 (2022)
2. Abdulrazzaq, N.T.; Abdul-Razzaq, K.S.: The effect of unequal load values on reinforced concrete deep beams. InBIO Web of Conferences 97 (2024)
3. Elsanadedy, H.M.; Al-Salloum, Y.A.; Almusallam, T.H.; Alshenawy, A.O.; Abbas, H.: Experimental and numerical

study on FRP-upgraded RC beams with large rectangular web openings in shear zones. Constr. Build. Mater. **194**, 322–343 (2019). https://doi.org/10.1016/j.conbuildmat.2018.10.238

4. Asghari, A.A.; Tabrizian, Z.; Beygi, M.H.; Amiri, G.G.; Navayineya, B.: An experimental study on shear strengthening of rc lightweight deep beams using CFRP. J. Rehabil. Civ. Eng. **2**, 9–19 (2014)
5. Al Rjoub, Y.S., Hamad, A.G.: Forced vibration of axially-loaded, multi-cracked Euler-Bernoulli and Timoshenko beams. Structures. **25**, 370–385 (2020). https://doi.org/10.1016/j.istruc.2020.03.030
6. Tsakmakis, C.; Broese, C.; Sideris, S.A.: Dynamics in explicit gradient elasticity: material frame-indifference, boundary conditions and consistent euler-bernoulli beam theory. Materials **17**(8), 17–60 (2024)
7. Demir, A.; Caglar, N.; Ozturk, H.: Parameters affecting diagonal cracking behavior of RC deep beams. Eng. Struct. **184**, 217–231 (2019). https://doi.org/10.1016/j.engstruct.2019.01.090
8. Campione, G.; Minafò, G.: Behaviour of concrete deep beams with openings and low shear span-to-depth ratio. Eng. Struct. **41**, 294–306 (2012). https://doi.org/10.1016/j.engstruct.2012.03.055
9. Nasser, K.W.; Acavalos, A.; daniel, H.R.: behavior and design of large openings in RC beams. ACI. J. **64**, 25–33 (1967)
10. Ashour, A.F.; Rishi, G.: Test of RC continuous deep beams with web openings. ACI Struct. J. **97**(3), 418–426 (2000)
11. Yang, K.H.; Eun, H.C.; Chung, H.S.: The influence of web openings on the structural behavior of RC high-strength concrete deep beams. Eng. Struct. **28**, 1825:1834 (2006)
12. Tan, K.H.; Tang, C.Y.; Tong, K.: Shear strength predictions of pierced deep beams with inclined web reinforcement. Mag. Concr. Res. **56**, 443–452 (2004). https://doi.org/10.1680/macr.2004.56.8.443
13. Hu, O.E.; Tan, K.H.; Liu, X.H.: Behaviour and strut-and-tie predictions of high-strength concrete deep beams with trapezoidal web openings. Mag. Concr. Res. **59**, 529–541 (2007). https://doi.org/10.1680/macr.2007.59.7.529
14. Jasim, W.A.; Tahnat, Y.B.A.; Halahla, A.M.: Behavior of RC deep beam with web openings strengthened with (CFRP) sheet. Structures. **26**, 785–800 (2020). https://doi.org/10.1016/j.istruc.2020.05.003
15. Salih, R.; Abbas, N.; Zhou, F.: Experimental and Numerical investigations on the cyclic load behavior of beams with rectangular web openings strengthened using FRP sheets. Structures. **33**, 655–677 (2021). https://doi.org/10.1016/j.istruc.2021.04.051
16. Nie, X.F.; Zhang, S.S.; Yu, T.: Behaviour of RC beams with a fibre-reinforced polymer (FRP)-strengthened web opening. Compos. Struct. **252** (2020). https://doi.org/10.1016/j.compstruct.2020.112684
17. Andermatt, M.F.; Lubell, A.S.: Strength modeling of concrete deep beams reinforced with internal fiber-reinforced polymer. ACI. Struct. J. **110**, 595–605 (2013). https://doi.org/10.14359/51685745
18. Andermatt, M.F.; Lubell, A.S.: Behavior of concrete deep beams reinforced with internal fiber-reinforced polymer-experimental study. ACI. Struct. J. 110, 585–594 (2013). https://doi.org/10.14359/51685744.
19. Al-Mahbashi, M.; Hussein, E.; Husain, A.; Aref, A.; Yousef, A.: Experimental and numerical study of high strength reinforced concrete continuous deep beams with circular and rectangular openings. J. Build. Eng. **79**. (2023)
20. Yousef, A.M.; Tahwia, A.M.; Al-Enezi, M.S.: Experimental and numerical study of UHPFRC continuous deep beams with openings. Buildings **13**(7), 17–23 (2023)
21. Manasa, K.V.; Jayaramappa, N.; Sai Nagendra, C.V.:Experimental and numerical study on flexural behaviour of deep beam with rectangular openings under static loading. In: International Conference on Interdisciplinary Approaches in Civil Engineering for Sustainable Development, pp. 337–350 (2023)

22. Frappier, J.; Mohamed, K.; Farghaly, A.S.; Benmokrane, B.: Behavior and strength of glass fiber-reinforced polymer—RC deep beams with web openings. ACI. Struct. J. (2019). https://doi.org/10.14359/51716774
23. Arabasi, S.; El-Maaddawy, T.: Reinforcing of discontinuity regions in concrete deep beams with GFRP composite bars. Compos. Part C. Open Access. **3** (2020). https://doi.org/10.1016/j.jcomc.2020.100064
24. Murugan, R.; Prasanna, G.: GFRP reinforced RC deep beam with multiple web openings. Adv. Civil Eng., pp. 453–469 (2020)
25. Tan, K.H.; Lu, H.Y.: Shear behavior of large RC deep beams and code comparisons. Struct. J. **96**, 836–846 (1999)
26. Rteil, A.; Alam, M.S.: Shear strength of RC deep beams—a review with improved model by genetic algorithm and reliability analysis. Structures **23**, 494–508 (2020). https://doi.org/10.1016/j.istruc.2019.09.006
27. El-Zoughiby, M.E.; El-Metwally, S.E.; Al-Shora, A.T.; Agieb, E.E.: Strength prediction of simply supported R/C deep beams using the strut-and-tie method, pp. 1973–1991(2013). https://doi.org/10.1007/s13369-013-0609-y
28. Ismail, K.S.; Guadagnini, M.; Pilakoutas, K.: Strut-and-tie modeling of RC deep beams. J. Struct. Eng. **144**, 1–13 (2018). https://doi.org/10.1061/(ASCE)ST.1943-541X.0001974
29. Sheikh-Sobeh, A.; Kachouh, N.; El-Maaddawy, T.: Performance prediction of GFRP-reinforced concrete deep beams containing a web opening in the shear span. Fibers **12**(8), 66 (2024)
30. Riyadh, M.; Hussein, A.; Al-ahmed, A.: Shear strength of RC deep beams with large openings strengthened by external prestressed strands. Structures. **28**, 1060–1076 (2020). https://doi.org/10.1016/j.istruc.2020.09.052
31. ACI. Building code requirements for structural concrete (ACI 318–19). American Concrete Institute (2019)
32. AASHTO. LRFD. Bridge design specifications. American Association of State Highway and Transportation Officials, Washington, DC (2012)
33. European Standard Norme Europeenne;1. (2011)
34. Fib, S.C.: Fib Structural Concrete, Textbook on Behaviour, Design, and Performance. International Federation for Structural Concrete, Lausanne (1999)
35. Sheikh, A.; Kachouh, N.; El-Maaddawy, T.: Numerical analysis of concrete deep beams reinforced with glass fiber-reinforced polymer bars. Buildings **13**(11), 27–67 (2023)
36. Heydari, P.; Mostofinejad, D.; Mostafaei, H.; Ahmadi, H.: Strengthening of deep RC coupling beams with FRP composites: a numerical study. Structures **51**, 435–454 (2023)
37. Shasikumar, J.N.; Sai Nagendra, C.V.:Experimental and numerical study on flexural behaviour of deep beam with circular openings under static loading. In: International Conference on Interdisciplinary Approaches in Civil Engineering for Sustainable Development, pp. 323–335, (2023)
38. Silveira, M.V.; Bitencourt, A.; Das, S.: Experimental and numerical investigation of large-scale reinforced concrete deep beams designed with the Generative Tie Method. Structures **58** (2023)
39. Cosenza, E.; Manfredi, G.; Realfonzo, R.: Development length of FRP straight rebars. Compos. Part B Eng. **33**, 493–504 (2002). https://doi.org/10.1016/S1359-8368(02)00051-3
40. Fava, G.; Carvelli, V.; Pisani, M.A.: Remarks on bond of GFRP rebars and concrete. Compos. Part B Eng. **93**, 210–220 (2016). https://doi.org/10.1016/j.compositesb.2016.03.012
41. Abbood, I.S.: Case studies in construction materials strut-and-tie model and its applications in RC deep beams: a comprehensive review. Case. Stud. Constr. Mater. **19**, e02643 (2023). https://doi.org/10.1016/j.cscm.2023.e02643
42. El-Metwally, S.; Wai-Fah, C.: Structural Concrete: Strut-and-Tie Models for Unified Design. CRC Press (2017)

43. Mohammadiasl, M.; Bagherieh, A.R.: Novel lower-bound solution for bearing capacity of RC deep beams. Pract. Period. Struct. Des Constr. **29** (2024). https://doi.org/10.1061/PPSCFX.SCENG-1314

44. Díaz, R.A.S.; Nova, S.J.S.; Teixeira, M.C.A.; Trautwein, L.M.; Almeida, L.C.D.E.: Reliability analysis of shear strength of RC deep beams using NLFEA. Eng. Struct. **203**,109760 (2020) https://doi.org/10.1016/j.engstruct.2019.109760

45. Zinkaah, O.H.; Ashour, A.; Sheehan, T.: Experimental tests of two-span continuous concrete deep beams reinforced with GFRP bars and strut-and-tie method evaluation. Compos. Struct. **216**, 112–126 (2019). https://doi.org/10.1016/j.compstruct.2019.02.078

46. Design CS.: Construction of Building Components with Fiber Reinforced Polymers (S806–12). Canadian Standards Association: Rexdale, ON, Canada. (2012)

47. CSA A23.3–14 C. Design of Concrete Structures Standard. Canadian Standards Association, Mississauga, ON, Canada, 240 (2014)

48. Sucharda, O.; Mateckova, P.; Bilek, V.: Non-linear analysis of an RC beam without shear reinforcement with a sensitivity study of the material properties of concrete. Slovak J. Civil Eng. **28**(1), 33–43 (2020)

49. Kubosek, J.; Vaskova, J.: Determination of material parameters for nonlinear analysis of reinforced concrete. Key Eng. Mater. **738**, 140–150 (2017)

50. Taqieddin, Z.N.: Elasto-Plastic and Damage Modeling of Reinforced Concrete. Louisiana State University and Agricultural ans Mechanical College. (2008)

51. Wu, H.; Lin, X.; Zhou, A.; Zhang, Y.X.: A temperature dependent constitutive model for hybrid fibre reinforced concrete. Const. Build. Mater. **15**, 109–130 (2023)

52. Drucker, D.C.; Prager, W.: Soil mechanics and plastic analysis or limit design. Q. Appl. Math. **10**(2), 157–165 (1952)

53. Ottosen, N.S.: A failure criterion for concrete. Am Soc Civil Eng Eng Mech Div J. **103**(4), 527–535 (1977)

54. William, K.; Warnke, E.: Constitutive Model for the Triaxial Behaviour of Concrete (1975)

55. Senthil K,; Sharma R.: Estimation on accuracy of compressive and tensile damage parameters of concrete damage plasticity model. In: International Conference on Wave Mechanics and Vibrations, pp. 65–76 (2022)

56. Al-Zuhairi, A.H.; Al-Ahmed, A.H.; Abdulhameed, A.A.; Hanoon, A.N.: Calibration of a new concrete damage plasticity theoretical model based on experimental parameters. Civil Engineering Journal. **8**(2), 225–237 (2022)

57. Shi, X.; Li, Q.; Li, B.; Zhou, J.: Simulation of mechanical properties of reinforced concrete beam based on ABAQUS. Adv. Front. Res. Eng. Struct. **1**, 62–67 (2023)

58. Faveryan, I.B.; Triwiyono, A.; Siswosukarto, S.: Numerical modeling of applied near-surface mounted on reinforcement slab with ABAQUS CAE. Jurnal Teknik Sipil. **17**(2), 78–83 (2023)

59. Xiao, H.; Zhang, K.; Du, J.: Numerical Simulation Analysis of Uniaxial Compression Damage of Reinforced Concrete Columns Based on ABAQUS **51**, 113–118 (2023)

60. Waghmare, A.; Ramaswamy, A.: Nonlinear analysis of reinforced concrete structural elements. Int. Assoc. Bridge Struct. Eng. IABSE, pp. 1419–1426 (2022)

61. Kenawy, M.; Kunnath, S.; Kolwankar, S.; Kanvinde, A.: Concrete uniaxial nonlocal damage-plasticity model for simulating post-peak response of reinforced concrete beam-columns under cyclic loading. J. Struct. Eng. **146**(5) (2020)

62. Mander, J.B.; Priestley, M.J.; Park, R.: Theoretical stress-strain model for confined concrete. J. Struct. Eng. **114**(8), 1804–1826 (1988)

63. Yong, Y.K.; Nour, M.G.; Nawy, E.G.: Behavior of laterally confined high-strength concrete under axial loads. J. Struct. Eng. **114**(2), 332–351 (1988)

64. Saenz, L.P.: Equation for the stress-strain curve of concrete. ACI J. **61**(9), 1229–1235 (1964)

65. Jian, L.: Based on ABQUS of concrete structure nonlinear finite element analysis. Adv. Mater. Res. **756**, 186–189 (2013)

66. Altaee, M.; Kadhim, M.; Altayee, S.; Adheem, A.: Employment of damage plasticity constitutive model for concrete members subjected to high strain-rate. Sustainable Development and Smart Planning. IMDC-SDSP. (2020)

67. Cheng, H.; Paz, C.M.; Pinheiro, B.C.; Estefen S.F.: Experimentally based parameters applied to concrete damage plasticity model for strain hardening cementitious composite in sandwich pipes. Mater. Struct. **53**, pp. 1–7 (2020)

68. Minh, H.L.; Khatir, S.; Wahab, M.A.; Cuong-Le, T.: A concrete damage plasticity model for predicting the effects of compressive high-strength concrete under static and dynamic loads. J. Build. Eng. **44** (2021). https://doi.org/10.1016/J.JOBE.2021.103239

69. Metwally, I.M.: Three-dimensional nonlinear finite element analysis of concrete deep beam reinforced with GFRP bars. HBRC journal. **13**(1), 25–38 (2017)

70. Jiang, S.; Yao, W.; Chen, J.; Cai, T.: Finite element modeling of FRP-strengthened RC beam under sustained load. Adv. Mater. Sci. Eng. (2018)

71. ABAQUS Theory Manual (Version 6.12). Dassault Systems SIMULIA Corporation. Providence. Rhode Island. USA (2012)

72. Altaee, M.; Cunningham, L.S.; Gillie, M.: Practical application of CFRP strengthening to steel floor beams with web openings: a numerical investigation. J. Constr. Steel Res. **155**, 395–408 (2019)

73. Mohamed, A.R.; Shoukry, M.S.; Saeed, J.M.: Prediction of the behavior of reinforced concrete deep beams with web openings using the finite element method. Alex. Eng. J. **53**(2), 329–339 (2014)

74. Shabanlou, M.; Mofid, M.; Tavakoli, A.: Post-fire performance of GFRP reinforced concrete deep beams: experimental and numerical study. Struct. Infrastruct. Eng., pp. 1–9 (2024)

75. Stoner, J.G.; Polak, M.A.: Finite element modelling of GFRP reinforced concrete beams. Comput. Concr. **25**(4), 369–382 (2020). https://doi.org/10.12989/CAC.2020.25.4.369